Supporting Online Material: Material and Methods

This document gives the implementation details of the numerical model of the central pattern generator presented in the main article (Section 1). Section 2 presents the design characteristics of the salamander robot. Section 3 explains the methods for measuring the kinematics of salamander and robot locomotion. Finally, Section 4 analyzes recent data that show that the limb oscillators intrinsically oscillate at lower frequencies than body oscillators.

1. Central pattern generator model

1.1 Nonlinear oscillator model and saturation function

An oscillator *i* is implemented with the following differential equations:

$$\dot{\theta}_i = 2\pi\nu_i + \sum_j r_j\ w_{ij} \sin(\theta_j - \theta_i - \phi_{ij}) \quad (1)$$

$$\ddot{r}_i = a_i\left(\frac{a_i}{4}(R_i - r_i) - \dot{r}_i\right) \quad (2)$$

$$x_i = r_i(1 + \cos(\theta_i)) \quad (3)$$

Where θ_i and r_i are the state variables of the oscillator, representing the phase and the amplitude respectively, ν_i and R_i determine the intrinsic frequency and amplitude (i.e., the frequency and amplitude towards which the oscillator converges when isolated), a_i is a positive constant determining how quickly the amplitude variable r_i converges to R_i. Couplings between oscillators are defined by the coupling weights w_{ij} and phase biases ϕ_{ij}. The phase bias determines the phase lag that the coupling tends to induce between oscillators.

Equation 1 determines the time evolution of the phases θ_i of each oscillator. As described in the next section, it ensures that if synchronization criteria are met, the oscillators will synchronize with phase differences that depend on the coupling parameters w_{ij} and ϕ_{ij}, and on the intrinsic frequencies ν_i. Equation 2 is a critically damped second order linear differential equation that ensures that the amplitude variable r_i will monotonically converge to the single point attractor R_i. This ensures that the amplitude of the oscillations will smoothly follow the parameter R_i even if this parameter is abruptly changed. Note that in Equation 1, the coupling terms are weighted by the variable r_j which means that an oscillator that has zero amplitude does not affect the phases of other oscillators. For each oscillatory center, an oscillating and positive

signal x_i is extracted representing the amplitude of the burst produced by the center (i.e., the instantaneous spike firing frequency of the motoneuron pool).

The *saturation function* $[\nu_i, R_i] = g(d_i)$ described in the article is mathematically defined as follows (see also Fig. S1, left):

$$\nu = g_\nu(d) = \begin{cases} c_{\nu,1}\, d + c_{\nu,0} & \text{if} \quad d_{low} \le d \le d_{high} \\ \nu_{sat} & \text{otherwise} \end{cases}$$

$$R = g_R(d) = \begin{cases} c_{R,1}\, d + c_{R,0} & \text{if} \quad d_{low} \le d \le d_{high} \\ R_{sat} & \text{otherwise} \end{cases}$$

Limb and body oscillators are provided with different saturation functions, with the limb oscillators systematically oscillating at lower frequencies than body oscillators for the same level of drive and saturating at a lower threshold (Fig. S1 left and Table S1). An isolated limb oscillator can thus oscillate from 0.2 to 0.6 Hz, and an isolated body oscillator from 0.5 to 1.3 Hz. Unless otherwise stated (e.g., for turning), all oscillators receive the same drive *d*.

Figure S1 (right) illustrates the activity of uncoupled body and limb oscillators when the drive is linearly increased during 40 seconds. At first (t<4s), while the drive remains below the lower thresholds (identical for both types of oscillators), no oscillations are induced. When the drive exceeds the lower thresholds d_{low}, slow oscillations start. The frequencies and amplitudes of the oscillations increase (at different rates) with the drive until the upper thresholds d_{high} are reached (first the limb oscillator at t=20s then the body oscillator at t=36s), in which case the oscillators saturate and their frequency and amplitude decrease to their saturation values.

1.2 Phase lag between two coupled oscillators

The phase lag between two coupled oscillators depends on the difference of their intrinsic frequencies and their coupling parameters. We here show the particular case of two oscillators coupled unidirectionally, with oscillator 2 projecting to oscillator 1:

$$\dot{\theta}_1 = 2\pi\nu_1 + r_2\ w_{12}\sin(\theta_2 - \theta_1 - \phi_{12})$$

$$\ddot{r}_1 = a_1\left(\frac{a_1}{4}(R_1 - r_1) - \dot{r}_1\right)$$

$$\dot{\theta}_2 = 2\pi\nu_2$$

$$\ddot{r}_2 = a_2\left(\frac{a_2}{4}(R_2 - r_2) - \dot{r}_2\right)$$

It is easy to demonstrate that the state variables r_1 and r_2 asymptotically converge to R_1 and R_2, respectively, from any initial condition. Since we are interested in determining whether these two oscillators will synchronize (i.e., evolve with a constant phase difference), and, if yes, with which phase difference, it is useful to introduce the phase difference $\varphi = \theta_2 - \theta_1$. The time evolution of the phase difference is determined by

$$\dot{\varphi} = f(\varphi) = \dot{\theta}_2 - \dot{\theta}_1 = 2\pi(\nu_2 - \nu_1) + r_2 w_{12} \sin(\varphi - \phi_{12})$$

If the oscillators synchronize, they will do so at the fixed points φ_∞ (i.e., points where $\dot{\varphi} = f(\varphi_\infty) = 0$):

$$\varphi_\infty = \arcsin\left(\frac{2\pi(\nu_2 - \nu_1)}{R_2 w_{12}}\right) + \phi_{12}$$

This equation has no solution if $\left|\frac{2\pi(\nu_2 - \nu_1)}{R_2 w_{12}}\right| > 1$, i.e., when the difference of intrinsic frequencies is too large compared to the coupling weight w_{12} multiplied by the amplitude R_2 of the oscillator 2. In this case, the oscillators do not synchronize, and are said to *drift* (i.e., their phases will increase at different rates). If $\left|\frac{2\pi(\nu_2 - \nu_1)}{R_2 w_{12}}\right| = 1$, the equation has a single solution, $\varphi_\infty = \frac{\pi}{2} + \phi_{12}$ if $\nu_2 > \nu_1$ and $\varphi_\infty = -\frac{\pi}{2} + \phi_{12}$ if $\nu_2 < \nu_1$. This solution is asymptotically stable, and the two oscillators will synchronize with that phase difference (i.e., they will phase-lock) from any initial phase values. If $\left|\frac{2\pi(\nu_2 - \nu_1)}{R_2 w_{12}}\right| < 1$, the equation has two solutions, one which is stable and one which is unstable. The stability of the fixed point is determined by the sign of $\frac{\partial f(\varphi_\infty)}{\partial \varphi} = R_2 w_{12} \cos(\varphi_\infty - \phi_{12})$. The fixed point is stable if this quantity is negative, and unstable if it is positive. If the initial phase difference is the unstable fixed point, the two oscillators will remain synchronized with that phase difference. In practice, we add a small noise term to the derivatives to push the system out these unstable points. For any other initial condition, the two oscillators will asymptotically synchronize to a phase difference corresponding to the stable fixed point. Arbitrary phase lags can thus be defined between two oscillators by adjusting the coupling parameters and/or the intrinsic frequencies of the oscillators. In particular, when the intrinsic frequencies of both oscillators are equal (like in our model of the body CPG), the phase difference is directly set by the phase bias ϕ_{12}.

In this particular case (two oscillators with unidirectional coupling), the coupling weight w_{12} does not affect the resulting phase difference, but only the speed of convergence towards it. In the general case with bidirectional couplings (or with additional couplings from other oscillators), the coupling weights are weighting factors that determine the influence of the different couplings on the resulting phase difference and on the common oscillation frequency.

1.3 Coupling weights and parameters used in the central pattern generator

As described in the main article, the complete CPG is made of 20 oscillators coupled together. Note that this is a simplified representation of the real CPG. For instance, salamanders have typically 40 segments in their spine, with two oscillatory centers per segment. The coupling weights and all other parameters used for our experiments are given in Table S1.

Setpoints for the robot joints are extracted from the CPG as follows. The body joint *k* receives the oscillatory desired angles (the setpoints) $\varphi_k = \alpha_k \ (x_{k\_left} - x_{k\_right})$, where x_{k_left} and x_{k_right} are the corresponding left and right oscillator outputs (see Fig. 1A in the main article). The parameter α_k is a gain that increases linearly from head to tail, from α_1=0.5 (the head spine motor) to α_6=1.0 (the tail spine motor). The desired angles are provided to standard PD controllers which control the torques produced by the motors. Using the difference between the two contralateral oscillators replicates how torques are produced by antagonist muscles along the body. Note that while the body CPG is made of 8 pairs of oscillators, only 6 of them project their signals as setpoints to the robot, because the robot's spine has only 6 actuated joints (See Fig. 1A in the main article). Since limb joints rotate permanently, their desired angles directly depend on the phase of the corresponding oscillator, i.e., $\varphi_k = g(\theta_{k\_limb})$, where g is a piece-wise linear function that is sub-linear for the angles corresponding to stance and supra-linear for the angles corresponding to swing. The speed of rotation is therefore slightly slower during stance, and slightly faster during swing. The slopes of g are adjusted such that stance lasts 40% of a complete cycle duration.

1.4 CPG activity during walking

Figure S2 (left) shows the CPG activity during a walking gait. At t=2.0s, limb oscillators rapidly synchronize with the phase relation of a trot, i.e., with contralateral limbs out of phase and diagonally opposed limbs in phase. The time to synchronize takes approximately half a cycle, as illustrated by the variations of instantaneous frequencies $\frac{\dot{\theta}_i}{2\pi}$ until t=3.5s. The couplings from the limb oscillators to the body oscillators force the body CPG to oscillate with an S-shaped standing wave. All oscillators on one side of the trunk and the tail oscillate approximately in phase, and trunk and tail oscillators are in

anti-phase. The standing wave is induced because the couplings from the limb oscillators to the body oscillators are stronger than the inter-oscillator couplings within the body CPG (which tend to generate traveling waves). In other words, the influence from the limb oscillators "overrides" the intrinsic tendency of the body CPG to produce traveling waves. Snapshots of the walking gait in the real salamander and the robot are shown in Fig. S2 (right). Movies S1.mov and S2.mov show the walking gaits of the salamander and robot.

Note that the body-limb coordination in both the robot and the real salamander is such that the forelimb on one side is maximally protracted (i.e. turned forward) when corresponding trunk segments are maximally flexed towards the other side (and similarly for the hindlimbs and the tail segments). This phase relation optimizes stride length, and the velocity of walking drops when other types of body-limb coordination are used. For instance, a walking gait where the spine is kept straight produces walking velocities approximately 35 % slower than gaits including the lateral standing wave undulations. Similarly, walking gaits in which the phase relations between limb and body oscillations are the opposite of those of the salamander produce velocities that are close to zero m/s. These findings support the idea that the specific body limb coordination exhibited by salamanders helps increasing walking velocities.

1.5 CPG activity during swimming and serpentine crawling gaits

Figure S3 (left) shows the CPG activity during swimming (or serpentine crawling). Since limb oscillators are saturated (zero frequency and amplitude), they do not influence the body CPG, and this releases traveling waves in the body CPG. In order to maintain the limbs horizontally along the body, the oscillators of the limbs need to be modified such that they converge to a specific constant phase (i.e., a specific angle) during swimming. The differential equation determining the phase of limb oscillators is thus extended as follows:

$$\dot{\theta}_i = 2\pi\nu_i + \sum_j r_j \; w_{ij} \sin(\theta_j - \theta_i - \phi_{ij}) + b_i \sin(\bar{\theta}_i - \theta_i)$$

where $\bar{\theta}_i$ is the rest angle of the limb (oriented backwards) and b_i is a gain that is set to zero when the drive is below the saturation threshold d_{high}^{limb} of the limb oscillators (walking), and set to 10.0, when it is above (swimming). The swimming mode in the salamander and in the robot is illustrated in Fig. S3 (right) and shown in movies S1.mov and S2.mov.

1.6 Turning

Figure S4 shows the activity of the CPG during turning, as described in the main article. When the difference between the left and right drive is not too large, the whole pool of oscillators keeps oscillating at a common frequency despite the differences in intrinsic frequencies (i.e., they remain synchronized). The asymmetry results only in a change of the oscillation amplitudes with the side receiving higher drive oscillating at higher amplitudes. This leads to an offset in the set points sent to the joint motor controllers, and the robot will turn towards the side receiving the highest drive. See also S2.mov.

2. Design characteristics of the salamander robot

The structure of the robot is modular with six modules for the spine, one module for the head, and two modules for the girdles. The density of the robot is slightly higher than that of water. The total length of the robot is 85 cm. Each module is waterproof and self-contained, with its own Li-Ion battery, PIC micro-controller (PIC16F876A), and actuator (except for the head module). Structural parts are molded using polyurethane. Actuation is provided by DC motors (Faulhaber 1724 T 003 SR IE2-512) with custom gearboxes (reduction factors of 125:1 and 60:1 for the spine and limb joints respectively). Motors are provided with 512-impulse per rotation encoders for joint-angle information. The spine modules have one degree-of-freedom (i.e., one actuator), and the leg modules have two degrees-of-freedom (one per limb). All axes of rotation in the spine are aligned (vertical axes). Like in some other robots (*S1, S2*), limbs are capable of continuous rotation with horizontal axes of rotation, perpendicular to those of the spine.

We use position control, with PD controllers embedded in each microcontroller for producing the torques necessary to follow the trajectories provided by the CPG model. The CPG model itself is implemented in a PIC microcontroller (PIC18F2580) in the head module, which is connected to the other module microcontrollers through an I^2C bus. The CPG is programmed in C. The Euler integration method with a 20 ms time step is used to integrate the system of coupled differential equations. Wireless communication on the 868 MHz ISM band is used to send the input signals d from a workstation to the CPG.

Our robot shares similarities with other biomimetic amphibious robots (*S2*-*S4*), as well as walking robots with flexible spines (*S5, S6*), but has the particularity that it combines the capability of anguilliform swimming, serpentine crawling (*S7*) and walking in a single robot.

3. Kinematic measurements of salamander and robot locomotion

We here describe how the kinematic measurements illustrated in Figs. 3 and 4 of the main article were realized.

Kinematic measurements of salamander locomotion

Animals

Four fully metamorphosed *Pleurodeles waltlii* obtained from Centre de Biologie du Développement (CNRS UMR 9925, France) were used. Their snout-vent lengths (SVLs) were 75 mm, 86 mm, 88 mm and 102 mm. The animals were kept in an aquarium at a constant temperature (18°C) which was the same as that used during the experiments. Under general anesthesia with tricaine methyl sulfonate (MS222, 1 g/l), 16 to 18 circular reflective markers (diameter: 3 mm) were glued to the skin along the dorsal midline. The rostro-caudal location of the markers was expressed as fraction of SVL. For each animal, 12 markers were glued between the 0.00 SVL (snout) and 1.00 SVL (vent) levels and one marker was glued on the tip of tail. Four to six additional markers were glued equally spaced along the tail, depending on its length. The animals were allowed to recover from anesthesia for 1-2h before kinematic recordings started. After recovery, the salamanders moved voluntarily or were induced to move by touching or gently squeezing the tail.

Video recording

Animals were videotaped in dorsal view during walking on a wet surface or swimming in a tank (working section: 25 cm x 45 cm). Video-taping was performed at 60 frames s^{-1} with a high-speed video camera (Peak 120 High Speed Video System). Parallax effects were negligible because the camera was placed a long distance from the working section (around 1 m) relatively to the width of the video field (approximately 30 cm). Scaling was performed from the known distance between two marks on track or on the tank.

Kinematic analyses

The *x-y* coordinates of the reflective markers were digitized in each frame with a video analysis software (Peak Performance Technologies) running on an IBM-compatible computer and imported into MATLAB to reconstruct the trajectory of each marker within the video field. A regression analysis was then performed to determine the overall direction of moving of the animal. For each video frame, the body midline profile was drawn using a linear interpolation of the *x-y* coordinates of the midline markers.

The forward speed of the animal was computed from movements of the most anterior midline marker (0.15 SVL) and converted to SVL per second ($SVL.s^{-1}$). Only locomotor periods in which the animal was moving in a straight line and at a constant speed were selected for further analysis. For the locomotor speeds observed (swimming: 1.14 to 2.90 $SVL.s^{-1}$; stepping: 0.43 to 1.00 $SVL.s^{-1}$), a selected locomotor period represented 2-6 complete locomotor cycles.

The *x-y* coordinates of midline markers and the parameters of the travelling line of the animal were used to compute the lateral displacement of each marker through time. The maximal amplitudes of the lateral displacement (Dmax) of each midline marker within

the locomotor cycle were then calculated as the distances between the maximal lateral excursion of that marker towards the left and right sides and the line of moving. The locomotor cycle was arbitrarily defined as the time interval between two successive maxima of the lateral excursion of the midline marker located at 0.80 SVL site (time resolution: ±16.7 ms).

Kinematic measurements of robot locomotion

A similar method was used to measure robot locomotion. The robot was filmed from above at 15 frames s^{-1} with a Basler A602fc-2 camera using a 8 mm C-mount lens. The frame data acquired over an IEEE1394 link was processed in real time with a custom program using the ARTag library to extract the *x*-*y* coordinates of the markers (sort of 2D barcodes, see Fig. S5) placed on the robot. The coordinates have been exported in CSV files and then imported in MATLAB for processing and analysis, like for the salamander.The tracking markers had a size of 55 x 55 mm. For walking, they were fixed on the top of the robot with double-sided adhesive tape. For swimming, they were fixed on a PVC support having the same size of the marker and placed 75 mm above the robot (using a rigid PVC cylinder of diameter 4 mm), to ensure that the markers were always out of the water during tracking. The measures were repeated five times for each drive level. For walking, the camera field of view was always containing two complete cycles; for swimming, this varied between two and five cycles.

Results reported in the main article (Figs. 3 and 4)

The results reported in the main article (Figs. 3 and 4) correspond to the measurements in one salamander individual (SVL=86mm, body length BL=190mm). For walking, 5 different sequences are recorded at various velocities (0.31, 0.31, 0.34, 0.35, 0.43 $BL.s^{-1}$). The lateral displacements (Dmax) are measured for each marker and averaged for a given sequence. The data points and error bars in Fig. 3 are the averages and standard deviations of the lateral displacements for the 5 different sequences. The snapshots in Fig. 3 correspond to the walking at 0.34 $BL.s^{-1}$ (0.75 $SVL.s^{-1}$). Since no markers were fixed to the limbs, limb movements and foot contacts have been estimated from visual inspection of the video. For swimming (Fig. 4), the same method is used based on 6 different sequences recorded at various velocities (0.52, 0.56, 0.62, 0.89, 0.92, 1.09 $BL.s^{-1}$). The snapshots in Fig. 4 correspond to the swimming at 0.89 $BL.s^{-1}$ (1.96 $SVL.s^{-1}$). Note that lateral displacements tend to increase slightly with the velocity during swimming. This is not the case during walking.

The robot lateral displacements were measured at drives equal to 1.0, 1.5, 2.0, 2.5, and 3.0 for walking, and drives equal to 3.01, 3.5, 4.0, 4.5, and 5.0 for swimming. Five runs were carried out for each level of drive. The lateral displacements (Dmax) are measured for each marker and averaged for the 5 runs at a given level of drive. The data points and error bars in Figs. 3 and 4 are the averages and standard deviations of the lateral displacements for the 5 different levels of drive. Similarly to the salamander, limb movements and foot contacts during walking (Fig.3B) have been estimated from visual inspection of the video.

4. Measuring the intrinsic frequencies of body and limb oscillators

During the design of the model, we hypothesized that the gap between the range of frequencies for walking and the range of frequencies for swimming could be due to differences in the intrinsic frequencies of limb and body oscillators. In particular, we hypothesized that limb oscillators have lower intrinsic frequencies than body oscillators (hypothesis 4), therefore slowing down the rhythms during walking, and, once silent, releasing faster rhythms during swimming. This hypothesis makes us predict that the motoneuron signals to limb and axial muscles should exhibit oscillations with different frequencies for the same tonic drive when the spinal cord is transected to isolate body oscillators from limb oscillators. An alternative explanation would be that limb and body oscillators have the same intrinsic frequencies for the same drive, but that higher centers ensure that the drive signal is never provided at intermediary levels (e.g., that the drive always makes a step increase during the switch from walking to swimming). We therefore used an *in vitro* brainstem-spinal cord preparation adapted from that previously developed in the adult urodele amphibian (*S8*) to test our prediction.

Animals (*Pleurodeles waltlii)* obtained from Blades Biological Ltd (United Kingdom) were kept in an aquarium at 17°C and fed twice a week. Surgical procedures, and handling and housing of the animals were in accordance with protocols approved by the INSERM Ethics Committee and conformed to NIH guidelines. Briefly, animals (n=5) were deeply anesthetized by immersion in a 0.1% aqueous solution of tricaine methanesulfonate (MS-222; Sigma). After evisceration, the entire brain was exposed, and the part rostral to the mesencephalon removed, in a dissection dish containing ice-cold amphibian Ringer solution (in mM : NaCl, 130; KCl, 2.1; $CaCl_2$, 2.6; $MgCl_2$, 0.2; HEPES, 4; glucose, 5; $NaHCO_3$, 1), saturated with O_2 (pH 7.4). Thereafter, a dorsal laminectomy was performed to expose the first 20 segments of the spinal cord, and the spinal cord was transected at the level of the obex. Two muscle nerves, one innervating the forelimb, and the other the hindlimb, were dissected free and cut.

The preparation was then pinned down, dorsal side up, in a Sylgard-lined chamber and superfused (5 ml/min) with cooled (7°C) and oxygenated amphibian Ringer's to which was added the irreversible neuromuscular blocking agent α-bungarotoxin (α-BGTX; Sigma; 2 μM). The preparation was kept under such conditions around 15 hours before the experimentation began. The day after, the temperature of the Ringer's solution was progressively raised to 17° C before recording procedures began.

Axial motor activities were recorded extracellularly, in a conventional way, from the 10^{th} or 11^{th} ventral root with glass suction electrodes, digitized, and stored on a computer hard disk (Cambridge Electronic Device micro 1401mk II). Limb motor activities were recorded extracellularly, in a similar way, from the central stumps of the dissected muscle nerves (Fig. S6, left). Once the control recordings were performed, the spinal cord was divided into three portions: rostral (1^{st} to 5^{th} spinal segments), middle (6^{th} to 12^{th} spinal segments) and caudal (13^{th} to 18^{th} spinal segments). The recording session started at least 1 hour after the transections.

Rhythmic motor activities were induced by adding 20 μM *N*-methyl-D-aspartate (NMDA, Sigma) to the superfusate together with 10 μM D-serine (Sigma). See (*S8, S9*). An interactive software (Spike2 for Windows) was used to determine the onset of ventral root or muscle nerve bursts of activity. The cycle duration of the axial motor rhythmicity was measured between successive bursts of ventral root discharges. The cycle duration of the limb motor rhythmicity was measured between successive bursts of nerve discharges.

Figure S6 shows that the 3 isolated portions of the spinal cord could display a rhythmic motor activity during bath co-application of NMDA (20 μM) and D-serine (10 μM). The bar graph in Fig. S7 (*bottom*) further shows that, in every animal, the mean frequency measured in the middle portion was significantly higher than that obtained in limb nerves (individual Kruskal-Wallis One Way ANOVA, $P<0.001$, Dunn's *post hoc*) (*right panel*), whereas the axial and limb frequencies were not significantly different (individual Kruskal-Wallis One Way ANOVA, $P>0.05$) in intact spinal cord preparations (*left panel*). It can thus be concluded that the intrinsic frequency of the segmental oscillators controlling the limb musculature is lower than that of the segmental oscillators controlling the axial musculature.

This is in good agreement with the CPG model. In the model, limb oscillators are intrinsically slower than body (axial) oscillators. When active simultaneously, the couplings from the limb oscillators slow down the oscillation frequencies in the body oscillators compared to their intrinsic frequency (Fig. S7 top left). When the couplings are removed (e.g., by setting the coupling weights to zero), the frequencies of the body oscillators return to their (higher) intrinsic frequencies (Fig. S7 top right), while the limb oscillators frequencies remain at their pre-transection value.

Note that the biological experiment also gives some support to the hypothesis 2, namely that couplings from limb oscillators to body oscillators are stronger than those from body oscillators to limb oscillators. Indeed for individuals 1, 2 and 3, the oscillation frequencies of the intact preparations are closer to those of the isolated limb oscillators than those of the isolated body oscillators, which is an indication of stronger influence of the limb oscillators in determining the common frequency when all oscillators are synchronized (for instance, the results of the model very closely match the measurements in the individual 1). More tests are needed to confirm this.

Supporting Online Material: Figures

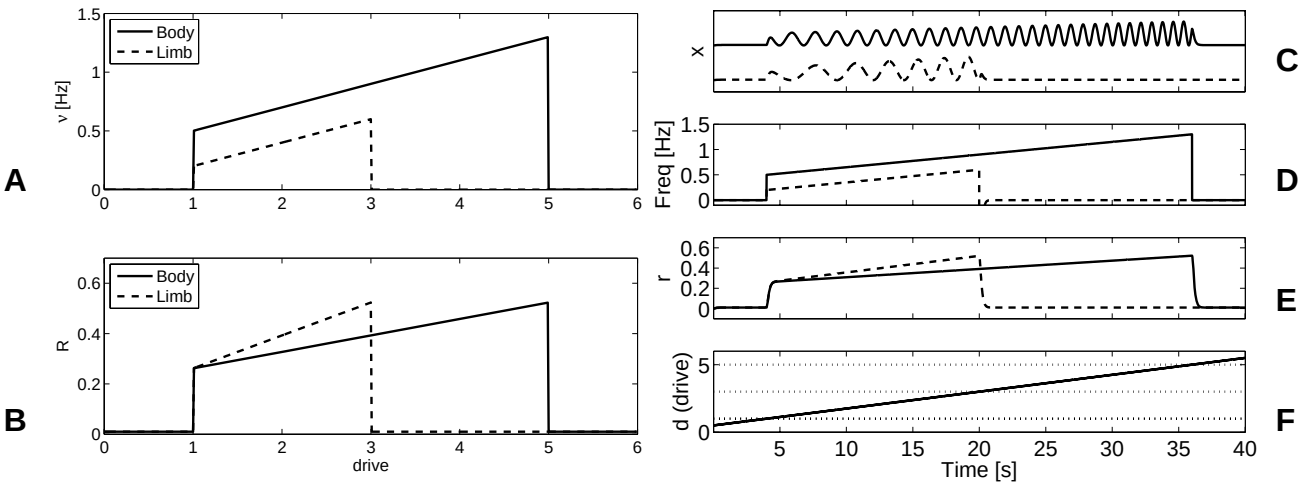

Fig. S1 Saturation function and oscillations in isolated (i.e., uncoupled) body and limb oscillators. *Left:* Saturation functions providing the intrinsic frequency ν (A) and amplitude R (B) for body and limb oscillators. *Right:* (C) Oscillations produced by the limb (dashed lines) and body (continuous lines) oscillators. (D) Instantaneous frequencies measured as $\frac{\dot{\theta}_i}{2\pi}$ in cycles/s. (E) Amplitude state variables r_i. (F) Drive signal. The horizontal dotted lines indicate the lower and higher thresholds of the saturation function (d_{low}^{limb} =1 and d_{high}^{limb} =3 for the limb oscillator; d_{low}^{body} =1 and d_{high}^{body} =5 for the body oscillator).

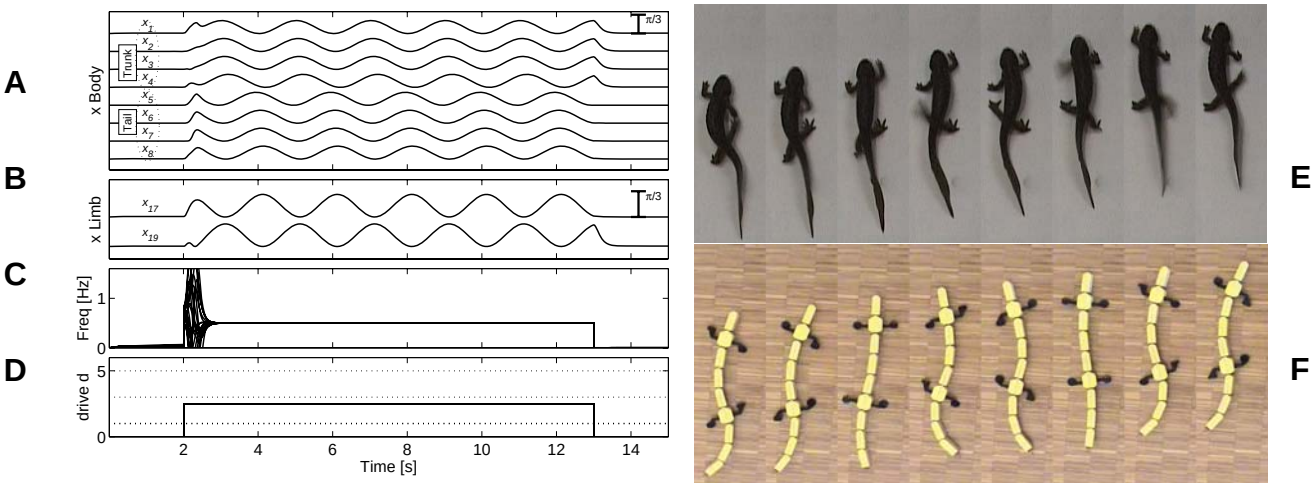

Fig. S2. *Left:* Activity of the CPG during walking. (A) x_i signals from the left body CPG oscillators. (B) x_i signals from the left limb CPG oscillators. (C) Instantaneous frequencies measured as $\frac{\dot{\theta}_i}{2\pi}$. (D) Drive *d* applied to all oscillators. *Right:* Walking gait with the real salamander (E) and the salamander robot (F). Note the standing wave in the body undulation. The sequences (approximately one period) last 0.84 s and 1.40 s, respectively. See also the movies S1.mov and S2.mov.

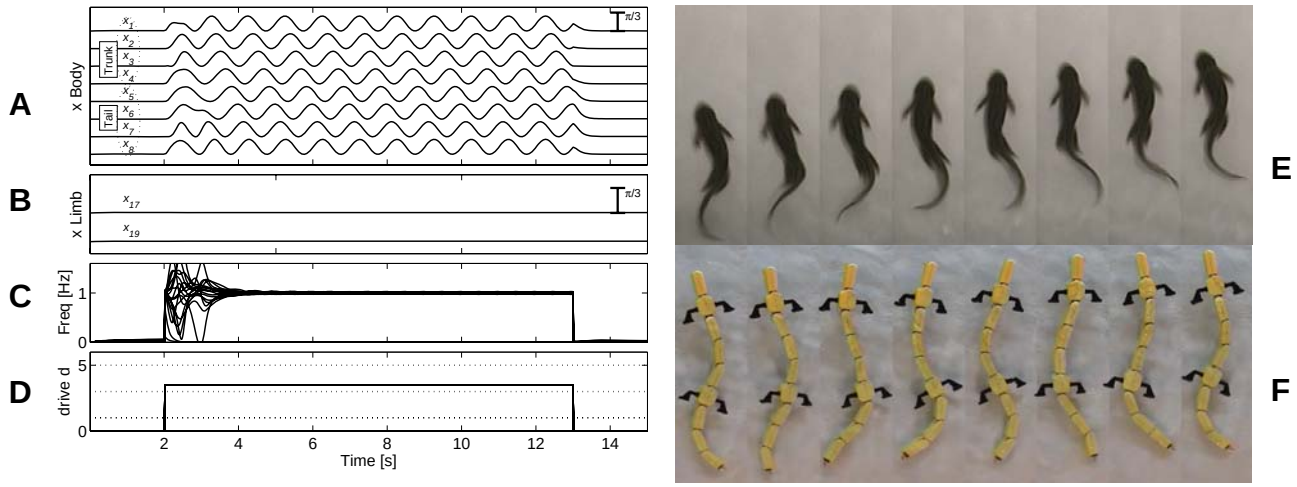

Fig. S3. ***Left:*** **Activity of the CPG during swimming. (A)** x_i **signals from the left body CPG oscillators. (B)** x_i **signals from the left limb CPG oscillators. (C) Instantaneous frequencies measured as** $\frac{\dot{\theta}_i}{2\pi}$ **. (D) Drive** ***d*** **applied to all oscillators.** ***Right:*** **Swimming mode with the real salamander (E) and the salamander robot (F). Note the traveling wave in the body undulation. The sequences (approximately one period) last 0.28 s and 0.84 s, respectively. See also the movies S1.mov and S2.mov.**

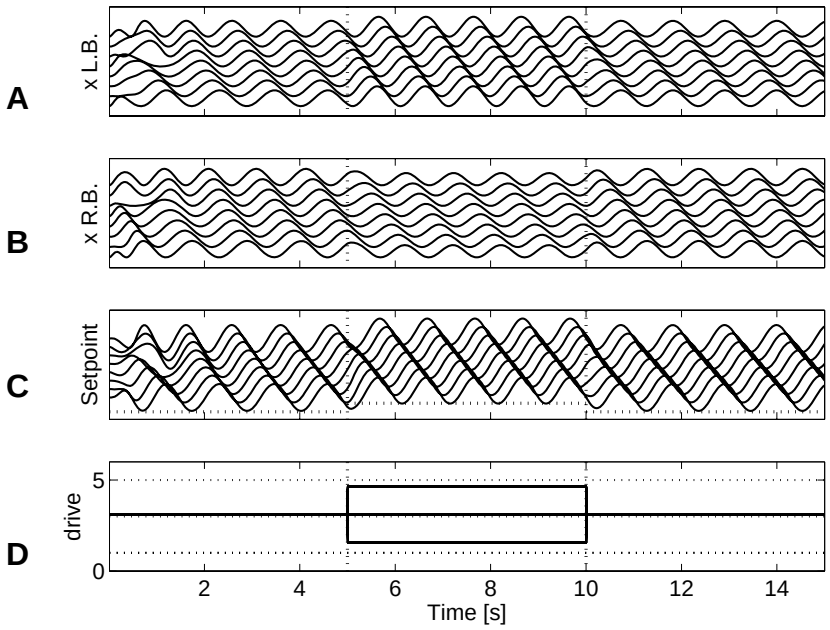

Fig. S4. Turning induced during swimming by asymmetrical drive between left and right sides of the body CPG. Outputs of the left (A) and right side (B) of the body CPG (LB and RB stand respectively for left and right sides of the body CPG). (C) Setpoints φ_k **sent to the motors. Notice the change of offsets of the setpoints for 5s<t<10s. (D) Drive signals applied to both sides of the body CPG.**

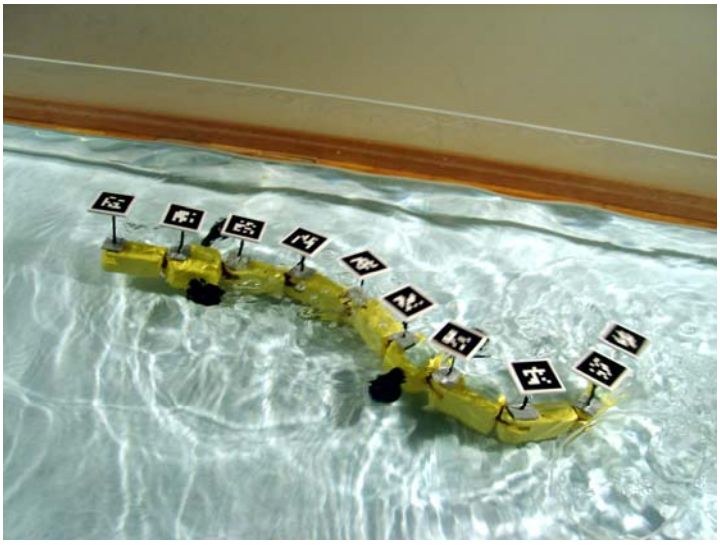

Fig. S5. The robot swimming in the aquarium with the tracking markers.

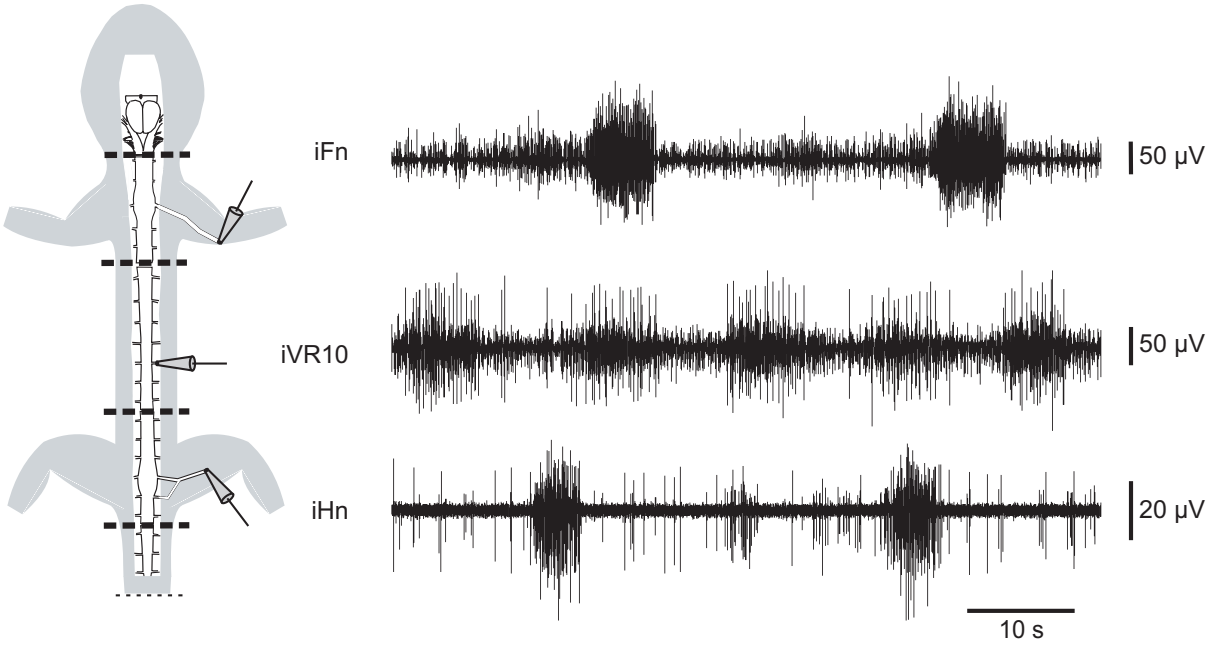

Fig. S6. Example of rhythmic motor activities induced in 3 isolated portions of salamander spinal cord by bath co-application of *N*-methyl-D-aspartate (20 µM) and D-serine (10 µM). Efferent activities (right panel) were recorded from a forelimb muscle nerve (iFn), the 10th ventral root (iVR10), and from a hindlimb muscle nerve (iHn) on the same side of the spinal cord. The dashed lines in the drawing of the preparation (left panel) indicate the levels of the spinal cord transections.

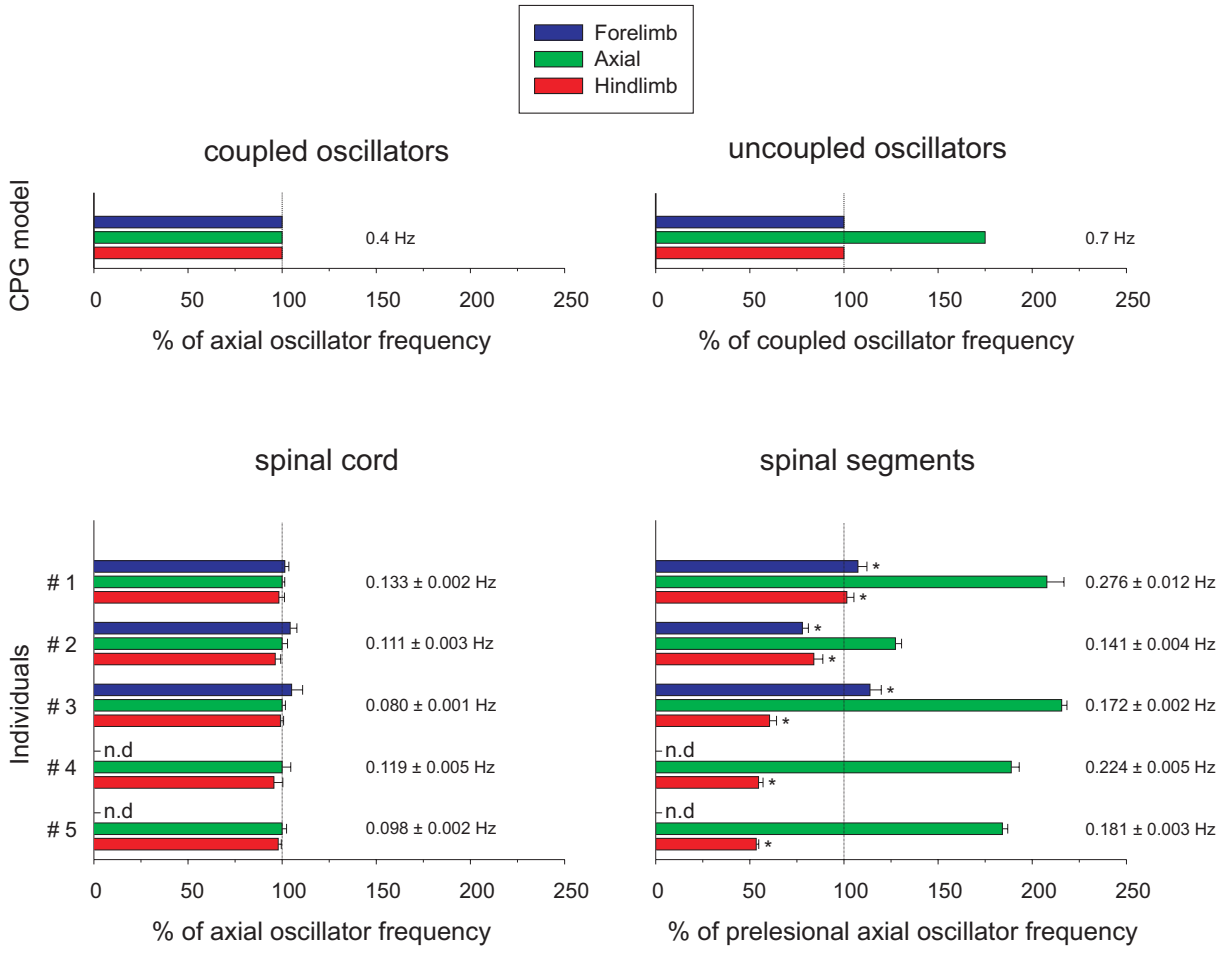

Fig. S7: ***Top*****: Frequencies of the limb and axial oscillators at drive d=2 when coupled as in the CPG model (left) and when isolated (right).** ***Bottom*****: Comparison between limb and axial oscillator frequencies in the intact spinal cord (*left panel*), and in spinal cord portions (*right panel*). For each individual, bars are expressed as a fraction of the axial mean frequency in the intact spinal cord. Error bars indicate SEM, and the numbers give the mean axial frequency ± SEM. *: *P*<0.05 vs. axial frequency, Dunn's post hoc. n.d. : no detectable efferent activity during the experiment.**

Supporting Online Material: Tables

Table S1: parameters used with the CPG model.

	Body oscillator	Limb oscillator
Number of oscillators	16	4
a_i in 1/s	20.0	20.0
$[d_{low}, d_{high}]$ in arbitrary units	[1.0, 5.0]	[1.0, 3.0]
$[c_{\nu,1}, c_{\nu,0}]$ in Hz	[0.2, 0.3]	[0.2, 0.0]
$[c_{R,1}, c_{R,0}]$ in radians	[0.065, 0.196]	[0.131, 0.131]
ν_{sat} in Hz	0.0	0.0
R_{sat} in radians	0.0	0.0
$[w_{ij}, \phi_{ij}]$ downwards in body CPG	[10.0, -2π/8]	
$[w_{ij}, \phi_{ij}]$ upwards in body CPG	[10.0, 2π/8]	
$[w_{ij}, \phi_{ij}]$ contralateral in body CPG	[10.0, π]	
$[w_{ij}, \phi_{ij}]$ from limb to body CPG	[30.0, π]	
$[w_{ij}, \phi_{ij}]$ within the limb CPG		[10.0, π]

Supporting Online Material: References and notes

S1. R. D. Quinn *et al.*, paper presented at the Climbing and Walking Robots Conference (CLAWAR01) 2001.

S2. U. Saranli, M. Buehler, D. E. Koditschek, *The International Journal of Robotics Research* **20**, 616 (2001).

S3. J. Ayers, J. Crisman, "The Lobster as a Model for an Omnidirectional Robotic Ambulation Control Architecture," *Biological neural networks in invertebrate neuroethology and robotics* 1993, pp. 287-316.

S4. H. Yamada *et al.*, paper presented at the 36th International Symposium on Robotics, Tokyo, Japan 2005.

S5. R. Breithaupt, J. Dahnke, K. Zahedi, J. Hertzberg, F. Pasemann, paper presented at the 5th International conference on Climbing and Walking Robots (CLAWAR2002), Paris, France 2002.

S6. A. Hiraoka, H. Kimura, paper presented at the Annual Conference of the Robotics Society of Japan, Osaka, Japan 2002.

S7. In some situations, e.g. during escape behavior in grass, the salamander uses a rapid serpentine crawling gait which amounts to swimming on ground. Similarly, the robot can "swim" on ground when elements providing asymmetric friction between the longitudinal and perpendicular axes (e.g. passive wheels) are attached to the body segments.

S8. I. Delvolvé, P. Branchereau, R. Dubuc, J.-M. Cabelguen, *Journal of Neurophysiology* **82**, 1074 (1999).

S9. M. Wheatley, M. Edamura, R. B. Stein, *Experimental Brain Research* **88**, 609 (1992).